JAST
Journal of Aerospace Science and Technology

Pages:88-100 / Vol. 16/ No. 1 /Winter- Spring 2023

Journal of Aerospace Science and Technology

www:jast.ias.ir

Scienctifie-Research Article

Determination of a High-speed Centrifugal Pump's Stable Performance Range by Computational Fluid Dynamics

Ali Cheraqi[1]*, **Reza Ebrahimi**[2]

1-2- Department of Aerospace Engineering, K. N. Toosi University of Technology, Tehran, Iran

ABSTRACT

Feed pumps play a crucial role in the dynamics of hydraulic systems. The surge phenomenon is a common type of instability in pumps and compressors. This phenomenon is a systematic instability and is influenced by the dynamics of all components of a hydraulic system, including tank, valves, suction pipes, impeller and the turbomachine itself. Surge emerges when a pump is operating with a positive slope of head and flow curve. The coincidence of the surge phenomenon with cavitation results in a damaging phenomenon called "auto-oscillation." Thus, predicting a pump's behavior outside the design points is of great importance particularly in low flow rates. In this paper, the characteristic curve of a high-speed centrifugal pump is extracted using CFD analysis to determine the stable operating range of the pump. The studied pump consists of an inducer, impeller and volute. The simulation in the pump was carried out three-dimensionally due to the asymmetry of geometry. The simulations are performed over a wide range of flow rates and the characteristic curve of the pump (head coefficient in terms of mass flow rate coefficient) is extracted. Finally, the range of stable operation of the pump is determined using its characteristic curve.

***Keywords**: centrifugal pump, instability, surge, CFD, the characteristic curve.*

Introduction

The possibility of occurring fluid-structure interaction is high and inevitable in hydraulic turbomachines. Even in the absence of cavitation and therefore avoiding its consequences, the phenomenon of fluid-structure interaction causes a faster decay of structure or, in a worst condition, the structure to break. According to the Electric Power Research Institute, these phenomena in boiler feed pumps have resulted in the incapacitation of pumps and interruption of energy generation in power plants. [1]

In contrast to cavitation, there is no inclusive source of scholarly works on the matter of instability in liquid turbomachines. The existing body of scholarly works on this matter precisely has described flow instability and recommended cautions to be taken into account during the design to prevent the aforementioned interruptions. Different parameters are involved in this regard, including vibration of blades and rotodynamic instabilities. When flow is low in a centrifugal pump, three different flow regimes can exist: stable regime, unstable regime, and transient regime. Having the pump in a stable performance

1 PhD. Candidate (Corresponding Author) **Email: *** Cheraqi@email.kntu.ac.ir
2 Professor

DOI : 10.22034/jast.2022.357423.1128
Submit: 26.08.2022 / Accepted: 24.12.2022
Print ISSN:1735-2134 Online ISSN: 2345-3648

48/ Journal of Aerospace Science and Technology
Vol.16/ No. 1/ Winter-Spring 2023

condition and avoiding unstable and transient regimes is always pursued. We will subsequently describe flow characteristics in these three regimes of flow. [2]

Stable regime

Most centrifugal pumps operate under a stable regime. The flow passing through the impeller is unilateral in this state. If cavitation incepts in this regime, vapor cavities are created in the impeller entrance, and after growing further, they collapse in the impeller channel. Observations have shown that these types of currents are stable at the macro scale. The inlet pressure of the pump is constant during pump operation. In this regime, the pump is only exposed to cavitation erosion.

Unstable regime

Cavitating Centrifugal pumps that can operate under an unstable regime are rare. This type of flow usually occurs when the flow and inlet pressure of the pump are low at the same time. Strong backflows occur at the pump inlet under this condition. The inducer's motions on cavities are induced during the operation, and cavities along the inlet duct's wall are returned outside before entering the impeller's eye. This hydraulic instability can cause drastic pressure oscillation. The condition gets more critical when the pump's inlet duct and impeller's geometry generate cavitating flows. The domain of pressure oscillation is predicted by the growth and collapse of bubbles inside the impeller that depend on NPSH and pre-rotation dependent on the pump's entrance and inlet ducts. This phenomenon is also known as "hydrodynamic cavitation surge."

Transient regime

When there is a low or near zero movement of volumetric flows between the fluid inside or near the impeller and the liquid inside the inlet duct, all the energy transferred to the fluid by the impeller is consumed for increasing the temperature. The coincidence of volumetric expansion with the increase of temperature results in increased pressure in the pump's entrance. Alternating flowback inside or near the blade inlet of impeller coincides with hydrodynamic induction surge in zero or almost zero flows. In this condition, the inlet pressure increases during the pump's performance. In pumps, this flow regime is called the "transient regime," also known as the "thermodynamic surge."

Surge instability

Considering what has been explained so far, we can say that cavitation surge is one of the possible instabilities in hydraulic structures. Surge occurs when the pump's flow rate is lower than the design flow rate, and the head and flow curve slope is positive. However, in the presence of cavitation, the surge phenomenon emerges even when the slope of head and flow curve is negative. This kind of surge coinciding with cavitation is known as the "auto-oscillation phenomenon." [1]

In Figure 1a, the characteristic curve of the pump's stable regime, i.e., head rise depending on mass flow rate, and the characteristic curve of the rest of the system's stable regime, i.e., head drop depending on mass flow passage, are shown. When the system is under a stable regime, the head rise in the pump equals the head rise in the rest of the system. Also, the flow passage should be equal in the pump and the rest of the system so that the pump can operate with the rest of the system at the crossing point O. In the present study, the pump's response to the decrease of flow passage to a level less than point O was examined. Due to this decrease, pump A caused more amount of head drop in the rest of the system. This head difference increased the flow passage and resulted in getting back to the normal point. In this condition, the slope of the pump's characteristic curve was lower than that of the rest of the system's characteristic curve. Hence, point O represents the quasi-static stable operating point. On the other hand, the system with the combination of pump B was quasi-statically unstable. This kind of instability is prevalent mainly in multiphase compressors. In Figure 1b, point A is stable, point B is neutrally stable and point C is unstable. The instability in point C causes oscillation in pressure and flow passage, a phenomenon called "surge."

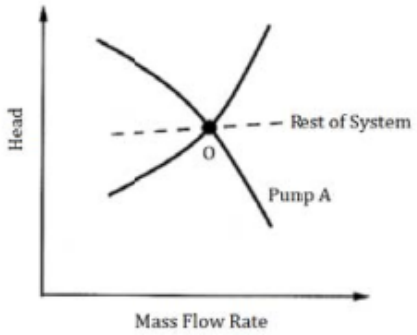

Figure 1b – Unstable and quasi-stable performance of systems with a pump

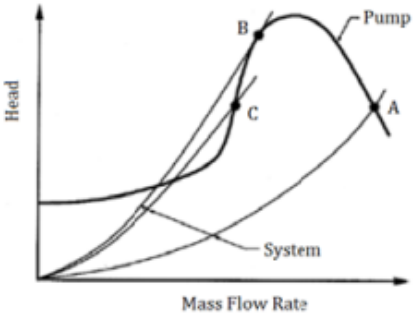

Figure 1a – Unstable and quasi-stable performance of systems with a pump [1]

Based on the definition of resistance, the following analysis was conducted for every serial component of the system.

$$R_i^* = \frac{d(\Delta H)}{d\dot{m}}$$

ΔH denotes quasi-static head drop of a component, i.e., the inlet head minus the outlet head, and is a function of the mass flow $\dot{m}$. According to the above analysis, the slope of the pump's characteristic curve in Figure 1a equals $-R^*_{Pump,}$ and the slope of the rest of the system's characteristic curve equals R^*_{System}. So, it can be concluded that the stability criterion is pursuant to the following inequality.

$$\sum_i R_i^* > 0$$

In other words, if the total value of the system's resistance is positive, then the system is quasi-statically stable. The above formula was interpreted based on the whole system's energy balance. Net energy flux to each component of the system equals $\dot{m}\Delta H$. Therefore, the net outlet energy of the system was calculated using the following equation.

$$\dot{m} \sum_i \Delta H_i = 0$$

at the stable point is equal to zero.

The system's stability was investigated by implanting a jamming device in a point of the system where the device increased the flow passage to the amount of $d\dot{m}$. E* denotes the new net energy flux toward outside the system and was calculated by the following equation.

$$E = \dot{d\dot{m}} \left[\sum_i \Delta H_i + \dot{m} \frac{d \sum_i H_i}{d\dot{m}} = \dot{m} d\, \dot{m} \sum_i R_i \right]$$

The value of E* is interpreted as the energy flux transferred to the system by the jamming device to rebalance the system. If the energy flux is positive E*, the first state of the system is stable. Hence, the above equation is a correct condition for stability. During the foregoing calculations, it was assumed that changes in the system occur slow enough that the pump and the rest of the system can follow the stable regime's characteristic curve. Thus, the above-mentioned analysis is efficient for low-frequency instabilities of the quasi-static domain. In higher frequencies, the inertia and compressibility of different elements of the flow should be considered.

Although quasi-static instabilities occur when R^*_i is smaller than zero, dynamic instabilities may also arise under a quasi-static stable condition in the system because if the resistance of a flow exceeds a particular quasi-static frequency, a complex function of frequency will be generated. Therefore, there may be different R^*_i resistances in frequencies higher than the quasi-static range. That being said, the value of dynamic resistance may be negative in some domains of frequency at some operating points. Under this condition, even if the system is quasi-statically stable, it cannot be dynamically stable. This description of dynamic instability seems strategic but oversimplified.

Literature review

A numerical study by Coutier-Delghosa et al. (2002) examined the effect of the leading edge shape on cavitation around inducer blade sections. Simulating cavitating flow on an inducer blade was done with two-dimensional hydrofoils. For liquid rocket engine inducer designs, two leading-edge shapes were selected. A numerical model of cavitating flows was developed using the three-dimensional code FINE/TURBOTM. Their study examined the cavitation process using a single

50/ Journal of Aerospace Science and Technology
Vol.16/ No. 1/ Winter-Spring 2023

fluid model in which liquid-vapor mixtures were modeled as homogeneous fluids whose density varied in proportion to static pressure. They then compared numerical results to experimental data. They also examined how the shape of the leading-edge influences on cavitation behavior. In another study (2003), the authors investigated the unsteady behavior of flow in inducer blades. [3]

Tokumasu et al. (2004) ran a numerical analysis to examine how flow properties influence cavitation's thermodynamic effect. Latent heat of vaporization causes a temperature depression of liquids that results in vapor pressure depression and suppression of cavity growth. It is known as the "thermodynamic effect of cavitation." Cryogenic fluids like LOX and LH2 are particularly prone to this effect. Considering the thermodynamic effect of cavitation, Tokumasu et al. numerically calculated the size of the cavity in a cryogenic fluid. Sheet cavities were assumed to exist. By analyzing the results, they examined the effect of liquid and Reynolds number properties on cavitation thermodynamics. [4]

Ugajin et al. (2006) used a 3D detached eddy simulator (DES) to simulate an unsteady cavitating flow in a turbopump inducer. Based on the source/sink of the vapor phase in the liquid flow, cavitation was modeled. Comparing the computational results with experimental measurements, and good agreement was found between them. Simulation of the unsteady motions of cavities was carried out in the inducer. Cavities extended and blocked the flow passage, leading to an increase in the magnitude of oscillation in cavity volume. It was shown that a tip-gap affected the cavity volume; the time-averaged volume of cavities for the inducer with the tip-gap was about five times that for the inducer without the tip-gap. They did not, however, examine unsteady phenomena, such as rotating cavitation and cavitation surge in the inducer. [5]

D. Pierrat et al. (2008) investigated leading edge cavitation in a helico-centrifugal pump experimentally and numerically. Experimental cavitation was observed on both sides of the impeller in their study, and head drop was measured under different operating conditions. Three flow rates, ranging from 0.85 Qn to 1.25 Qn, were simulated using a CFD model and compared with experimental results. The numerical and experimental cavitation figures were in good agreement. [6]

Yamamoto and Tsujimoto (2009) examined how backflow vortex cavitation affects cavitation instabilities. Cavitation instabilities in turbomachinery, such as cavitation surge and rotating cavitation, are commonly attributed to cavitation's quasi-steady characteristics, mass flow gain factor, and cavitation compliance. Yet, there are certain circumstances in which unsteady characteristics need to be taken into account. An example of a cavitation surge in industrial centrifugal pumps was used to demonstrate the significance of the phase delay of backflow vortex cavitation. A description of the backflow vortex structure was first given, and then the energy transfer during the cavitation surge in a centrifugal pump was discussed. Then, to explain the phase lag observed in the experiment, they discussed the dynamics of backflow. [7]

Kang and Yonezawa (2009) examined the cause of cavitation instabilities in a three-dimensional inducer. They simulated alternate blade cavitation, rotating cavitation, and cavitation surge in rocket turbopump inducers using a commercial code. The velocity disturbance caused by cavitation was determined by extracting the velocity vector under a non-cavitating condition from that under a cavitating condition for clarifying the cause of cavitation instabilities. They found that a disturbance flow there exists towards the trailing edge of the tip cavity. This flow had an axial flow component towards downstream which decreased the incidence angle for the next blade. Cavitation instabilities are found to start occurring when this flow interacts with the next blade. Experiments proved that disturbance flows exist. [8]

Using numerical methods, An and Shin (2011) analyzed the vortices behavior of the internal flow through a centrifugal pump, examining the formation and shedding of cavitation. A full three-dimensional flow was calculated utilizing structured mesh for a six-blade impeller in a single-section centrifugal pump. The boundary condition was a constant suction vortex. The variable flow rates of two pump systems with and without suction vortices were examined to determine the behavior of the vortices. Based on the results, suction vortices induced biased flow structure and more cavitations, particularly at the low flow rate condition. An investigation and discussion were conducted on complicated internal flow phenomena through impellers, such as cavitation formation and shedding, vortex growth,

separation of the flow, and flow instability due to suction vortices. [9]

Simulating cavitation inception in a radial-flow pump was carried out numerically by Somashekar and Purushotham in 2012. They provided experimental evidence of cavitation inception in a radial-flow pump operating at 1500rpm, with a head of 21m and a discharge pressure of 26lps at its best efficiency point (BEP). The numerical analyses were carried out using ANSYS13 and CFX software. The pump's cavitation breakdown curve and performance characteristic curve were obtained. [10]

Using numerical simulations and experimental investigations, Campos-Amezcua et al. in 2013 tested cavitating flow through an axial inducer that considered the tip clearance. In particular, they investigated the effect of the radial tip clearance on cavitation behavior. Numerical analyses were conducted on two different configurations. Initially, the inducer was modeled without considering tip clearance. Subsequently, it was modeled with nominal tip clearance and modified accordingly. The small size of the inducer caused the radial tip clearance to have a significant effect on the overall inducer performance in the non-cavitating regime. In addition, they found out that the influence of radial tip clearance is significant as well in cavitation behavior. Numerical results and experimental data, both with nominal tip clearance, were discussed in the context of cavitating and non-cavitating regimes. [11]

Fu et al. (2015) conducted a numerical and experimental study of flow in a centrifugal pump undergoing low flow rates. They, in particular, applied a three-dimensional simulation of internal flow through and long portions of the pump inlet and outlet ducts. During the experiments, high-speed digital movies were used to visualize the internal flow patterns, and fast response pressure transducers were used to examine the inlet pressure pulsations close to the impeller eye.

Based on the experiment results, the internal flow of the centrifugal pump operating at low flow rates exhibits a peculiar low-frequency oscillation. On the other hand, the low-frequency pressure fluctuations were closely related to flow instabilities induced by cavitation presence at low flow rates. In conclusion, the hydraulic performance of the centrifugal pump predicted by numerical simulations was in good agreement with that observed experimentally. [12]

According to Mishra and Ghosh (2015), a CFD model predicted the performance of the axial pump inducer for a staged combustion cycle-based rocket engine. Using ANSYS® CFX, a steady-state CFD analysis of liquid oxygen (LOX) axial pump used as a booster pump for an oxygen-rich staged combustion cycle rocket engine was presented in their paper. The LOX pump inducer's performance characteristic curves were obtained. Using the formalism, they could predict the inducer performance for a range of throttling from 80% to 113% of nominal thrust and for rotational speeds ranging from 4500 to 7500 rpm. Several simulations were carried out to determine the region of cavitation inception under different inlet pressure. [13]

A study by Guo et al. in 2016 examined how the number of inducer blades affects both the anti-cavitation characteristics of centrifugal pumps and their external performance. A vapor-liquid flow was simulated in a centrifugal pump using Rayleigh-Plesset equations and the mixture model, and its external performance was then predicted. They also tested the external performance of a centrifugal pump equipped with 2-, 3-, and 4-bladed inducers. Experiments were conducted with the three inducers, and the numerical results were validated. Their study found that a centrifugal pump with a 3-bladed inducer had a greater vapor volume fraction than one with a 2- or 4-bladed inducer, which indicates that the 3-bladed inducer has a better anti-cavitation performance. [14]

Given what has been said so far, predicting pumps' behavior and performance in the points outside the design is crucial in pump design, manufacturing, and ensuring a steady performance of pumps in pump-based systems. Experimental methods are the most accurate but costly way to obtain a characteristic curve. The present paper demonstrates the extraction of a high-speed feed pump's characteristic curve through computational fluid dynamics. The feed pump used in this study consisted of an inducer, impeller and volute. The inducer was implanted to increase inlet flow pressure entering the impeller and prevent cavitation inception in the impeller's eye. A single-stage numerical analysis was conducted. The numerical results are compared to this feed pump's existing experimental data. A difference between the numerical results and experimental data was detected that is due to the simplification of the

52/ Journal of Aerospace Science and Technology
Vol.16/ No. 1/ Winter-Spring 2023

pump's geometry during the numerical computations.

Losses in turbomachines fall into two categories, including internal and external losses. Internal losses include hydraulic losses, internal and wall or disk leakage. External losses include mechanic losses and external leakage. During numerical calculations of flow to simplify the pump's geometry, some pump elements, including leakage passages, seals, and leakage return passages, were eliminated from the original geometry. The pump's efficiency increases due to this elimination and consequently skipping over leakage and disk losses. Therefore, the existing difference between numerical and experimental results is acceptable, and numerical analysis results can be counteracted based on the losses mentioned above.

Performance characteristic curve

Pump's performance test is the main experiment for pumps. This test determines shortcomings of a pump's design and manufacturing. Through this test, performance and characteristic curves of the pump are obtained, and parameters such as vibrations, flow rate, head, and power consumption are measured in five operating points based on the API610 Standard. The measured data should be plotted in a spline curve or a third- or fourth-degree polynomial graph. Head and power of allowable operating point is calculated using the API610 Standard. The calculated value of velocity, viscosity and density should be modified for correction. [15]

On the other hand, quasi-experimental relationships are one of the best methods available to predict the performance of pumps. These relations are based on numerous experiments on various pumps and approximates head-flow characteristic curves through a second-degree equation. This equation has three variables. It represents the relationship between head and flow coefficient and is used with different rotational speeds. These equations depend on geometric specifications and values of pump design. By accessing real data of a specific point like the operating point determined by experiments, other points of the head will be determined based on flow rate. We do not demonstrate the details of calculations of these coefficients in the present paper. The foregoing equation is presented below.

$$\frac{H}{\omega^2} = A + B\left(\frac{Q}{\omega}\right) + C\left(\frac{Q}{\omega}\right)^2$$

There are similar equations to this foregoing equation for predicting efficiency. The results obtained from these equations are accurate, especially when employing them near of design point (the real value obtained from the test). Thus, this equation is not accurate in points further than the design point or in downstream.

The numerical analysis

In the present study, the characteristic curve of a feed high-rotational speed pump was obtained by a numerical analysis and compared to experimental results. The results obtained from the numerical analysis were used to determine the range of the pump's steady performance. The development of numerical methods has introduced CFD as a dominant method to examine flows inside pumps. The numerical analysis was performed in this study through the CFD commercial code. The turbomachine in which we simulated a flow consisted of an inducer, impeller, and volute. The simulation was performed using static and dynamic coordinate systems simultaneously and the Moving Reference Frame model.

Governing equations

Two ways to present continuity and momentum equations for a single-phase fluid flow are given below. [16]

$$\frac{\partial \rho}{\partial t} + \frac{\partial}{\partial x_j}\left(\rho U_j\right) = 0$$

$$\frac{\partial(\rho U_i)}{\partial t} + \frac{\partial}{\partial x_j}\left(\rho U_i U_j\right) = -\frac{\partial p'}{\partial x_i} + \frac{\partial}{\partial x_j}\left[\mu_{eff}\left(\frac{\partial U_i}{\partial x_j} + \frac{\partial U_j}{\partial x_i}\right)\right] + S_M$$

The resultance of body forces is represented by S_M, the viscosity effect is represented by μeff, and the modified pressure is represented by p'. To calculate Coriolis and centrifugal forces for rotating systems with constant angle ω, more source expressions must be used.

$$S_M = -2\rho\vec{\omega} \times \vec{U} - \rho\vec{\omega} \times (\vec{\omega} \times \vec{r})$$

Based on the equation above, the first expression results from centrifugal forces, while the second results from Coriolis force.

Turbulence modeling

Commercial codes use different turbulence simulation models. However, there is no integrated model applicable to all turbulent flows. The choice of turbulence model is made depending on factors such as governing physics, computation accuracy, meshing grid quality, and computational facilities. There are several advantages of two-equation models over other models, including their compatibility with numerical methods and their accuracy and reliability in computing.

The $k-\varepsilon$ model is the most popular two-equation model. Several works have been devoted to optimizing this model since its strengths and weaknesses are well known. If there is a flow with an adverse pressure gradient, the $k-\omega$ model is more efficient than the $k-\varepsilon$ model. Since the $k-\varepsilon$ model is a high-Reynolds model, it is inefficient in areas close to the wall, i.e., the low-Reynolds area. Using dense elements, on the other hand, the $k-\varepsilon$ model successfully predicts flow behavior near walls. [17]

In two-equation models, the turbulent velocity scale is calculated based on turbulence kinetic energy. The turbulence kinetic energy itself is achieved by solving its transfer equation. The turbulent length scale is estimated based on two characteristics of the turbulence field, including kinetic energy and turbulence dissipation rate. The dissipation rate of turbulence kinetic energy is achieved by solving its transfer equation.

K denotes turbulence kinetic energy and is defined as the variance in oscillations of velocity and ε denotes the dissipation of turbulent vortex (dissipation rate of oscillations of the velocity). Two-equation models are established based on the concept of vortex viscosity.

$$\mu_{eff} = \mu + \mu_t$$

The $k-\varepsilon$ model assumes that turbulent viscosity has a relationship with kinetic energy and turbulence dissipation rate through the below equation in which c_μ has a constant value.

$$\mu_t = C_\mu \rho \frac{k^2}{\epsilon}$$

The values of k and ε are directly calculated by equations of differential transfer of kinetic energy and turbulence dissipation rate.

$$\frac{\partial(\rho k)}{\partial t} + \frac{\partial}{\partial x_j}(\rho U_j k) = \frac{\partial}{\partial x_j}\left[\left(\mu + \frac{\mu_t}{\sigma_k}\right)\frac{\partial k}{\partial x_j}\right] + P_k - \rho\varepsilon + P_{kb}$$

$$\frac{\partial(\rho\varepsilon)}{\partial t} + \frac{\partial}{\partial x_j}(\rho U_j \varepsilon) = \frac{\partial}{\partial x_j}\left[\left(\mu + \frac{\mu_t}{\sigma_\varepsilon}\right)\frac{\partial \varepsilon}{\partial x_j}\right] + \frac{\varepsilon}{k}(C_{\varepsilon 1} P_k - C\varepsilon 2\rho\varepsilon + C\varepsilon 1 P\varepsilon b$$

$C_{\varepsilon 1}$, $C_{\varepsilon 2}$, σ_k and σ_ε are constant. P_{kb} and $P_{\varepsilon b}$ consist of buoyancy forces and are obtained by the below equation. P_k denotes turbulence production through viscous forces and is calculated through the equation below.

$$P_k = \mu_t\left(\frac{\partial U_i}{\partial x_j} + \frac{\partial U_j}{\partial x_i}\right)\frac{\partial U_i}{\partial x_j} - \frac{2}{3}\frac{\partial U_k}{\partial x_k}\left(3\mu_t\frac{\partial U_k}{\partial x_k} + \rho k\right)$$

The value of $\partial U_k/\partial x_k$ is small in an incompressible flow, and the second expression on the right side part of the above equation does not have a significant effect on production. The value of $\partial U_k/\partial x_k$ in a compressible flow is only significant in high-divergent areas like shocks. The expression $3\mu t$ in the above equation prevents an excessive increase of k and ε values in shocks.

Pkb ,i.e., buoyancy production, is established as follows when using the full buoyancy model.

$$P_{kb} = -\frac{\mu t}{\rho\sigma_p} g_j \frac{\partial \rho}{\partial x_i}$$

But when using the Boussinesq model, P_{kb} is established as follows.

$$P_{kb} = -\frac{\mu_t}{\rho\sigma_p}\rho\beta g_i \frac{\partial T}{\partial x_i}$$

One advantage of the $k-\omega$ model is its potential to optimize calculations near the wall in low-Reynolds areas. This model does not include non-linear damping and complex functions that the $k-\varepsilon$ model requires. This is another feature that makes the $k-\omega$ model more accurate. The low-Reynolds $k-\varepsilon$ model requires a high resolution of $y^+<0.2$ in the area near the wall. In contrast, the resolution of $y^+<2$ suffices in the the $k-\omega$ model. It is worth noting that in industrial flow simulations providing even a resolution of $y^+<2$ is not an easy task. Therefore, a new wall function has been developed for the $k-\omega$ model. This model constantly shifts from low-Reynolds to wall

54/ Journal of Aerospace Science and Technology
Vol.16/ No. 1/ Winter-Spring 2023

function. The $k-\omega$ model assumes that turbulent viscosity is related to turbulence kinetic energy and turbulent frequency through the equation below.

$$\mu_t = \rho \frac{k}{\omega}$$

Wilcox presented this formula. By means of this method, two transfer equations are solved, including one for k, the turbulence kinetic energy, and another for ω, the turbulent frequency. The tenor of the stress is calculated based on the viscosity-vortex concept.

$$\frac{\partial(\rho k)}{\partial t} + \frac{\partial}{\partial x_j}(\rho U_j k) =$$
$$\frac{\partial}{\partial x_j}\left[\left(\mu + \frac{\mu_t}{\sigma_k}\right)\frac{\partial k}{\partial x_j}\right] + P_k - \beta'\rho k\omega + P_{kb}$$
$$\frac{\partial(\rho\omega)}{\partial t} + \frac{\partial}{\partial x_j}(\rho U_j \omega) =$$
$$\frac{\partial}{\partial x_j}\left[\left(\mu + \frac{\mu_t}{\sigma_\omega}\right)\frac{\partial \omega}{\partial x_j}\right] + \alpha\frac{\omega}{k}P_k - \beta\rho\omega^2 + P_{\omega b}$$

P_k denotes turbulence production rate which is calculated in the same way as in the $k-\varepsilon$ model. The coefficients of this equation are presented in different scholarly works.

A model called SST, which combines the advantages of both models mentioned, is used to enjoy the benefits of both models in working with low and high Reynolds numbers. In flow regimes with adverse pressure gradients, the SST model is more accurate and reliable. Due to switching from one primary model to another, this model may suffer from instabilities or weak convergence, even though it enjoys the benefits of both primary models. We opted to use the SST model in the present study. The $k-\varepsilon$ and $k-\omega$ models use the gradient-diffusion hypothesis to connect the Reynolds stresses and average-velocity gradient to turbulent viscosity. The turbulent viscosity is modeled as a product of turbulent velocity and turbulent length scale.

Approximation of advection term

Analytical solving of Navier–Stokes equations is possible only for some flows under ideal conditions. In the present study, the actual flow was solved by replacing governing equations with algebraic approximations and by means of numerical methods. CFX used the element-based finite volume method. First, the solution field was meshed. The purpose behind meshing was to generate finite volumes to ensure the continuity of dependent quantities such as mass, momentum, and energy. Meshing is usually conducted three-dimensionally, but we did it two-dimensionally in order to simplify the process. Figure 1 demonstrates the two-dimensional grid. All solution variables and fluid properties were saved in knots.

There are different formulas for the discretization of commutative expressions. The following is the most common way of discretization. [16]

$$\varphi = \varphi_{up} + \beta\nabla_\varphi \cdot \Delta\vec{r}$$

φ_{up} denotes the value of φ quantity in upstream node, $\vec{r}$ denotes the vector between the upstream node and calculate node. $\beta\nabla\varphi \cdot \Delta\vec{r}$ denotes correction of numerical shift and has an anti-diffusion property, and is added to the wind-facing design. $\beta = 0$ results in a first-order upwind design and $\beta = 1$ results in a high-accurate second-order design.

In the present study, the High-Resolution design was employed. This design uses a non-linear algorithm to calculate β in every node. This design is more efficient than the second-order upwind design in preventing nonphysical oscillations and improving convergence rate. [4]

Velocity-pressure correlation

The Navier–Stokes equations lack an equation specific to pressure, and this makes solving them complicated. On the other hand, the continuity equation lacks a governing variable in incompressible flows. So, mass conservation is more of a kinematic constraint on velocity field than a dynamic equation. One way to compensate for these shortcomings is to design a pressure field to preserve the continuity equation. This may sound unusual, but considering that pressure does not have a crucial influence in an incompressible flow and this is the pressure gradient that is significantly influential, the practicality of the above-suggested solution becomes obvious. The continuity equation is efficient in calculating density in compressible flows but inefficient for incompressible or low-Mach-number flows. In compressible flows, the pressure is calculated by the equation of state.

In CFX, all variables are placed at equal points and with equal volumes allocated to them. Since many

expressions of different equations are recurrent, the number of coefficients required to be calculated and saved is minimized. This is actually a sympatric design frequently used in complex solution domains. Due to the problems caused by the lack of correlation between velocity and pressure and oscillation inception, the sympatric design was not used in computations of incompressible flows. From the mid-1960 in which allopatric nets were introduced until early 1980, in which velocity-pressure relation algorithms got famous, the sympatric designs gained attention. CFX uses the method of the sympatric net with equal control volume for all discretization equations. According to Patankar, the sympatric designs result in a lack of pressure field correlation. [16] Ray and Cho presented an alternate discretization for mass flows coupled with pressure and velocity. Mujumdar adjusted this discretization to eliminate problems of constant solution by time step.

Computational domain and mesh generation

In the present study, a flow simulation was performed in a high-speed feed pump. The geometry used in the present study consisted of an inducer, impeller and a volute. SOLID software was used to generate the geometry of the pump. The model's fluid field was determined before running the CFD analysis. A rotating part, including an inducer and an impeller, and a nonrotating part, including a volute, inlet and outlet ducts, comprised the solution field. To achieve better convergence, the volute was equipped with an outlet duct. Figure 1 demonstrates the solution field.

Gambit developed the grid of the solution field. We developed three different grids with a different number of meshes, and we performed numerical analyses at the design point to find the best grid. A comparison of the specifications of the generated grids and the parameters that influenced the mesh quality of the three grids is shown in Table 1. This table represents numbers as percentages. Based on the results of analyses on the second and third grids, these grids' head coefficients were not significantly different; therefore, the second grid was used for analyzing other operating points in order to reduce the computation costs. Figure 2 shows a sample of generated mesh on the inducer and impeller surfaces.

As there were a large number of computations in this study, we used parallel processing. Mesh and condition settings were completed by the MeTiS separator, the solution field was divided into 32 computational areas, and a processor analyzed each area.

Figure 2 – computational domain for flow calculation passing through the pump

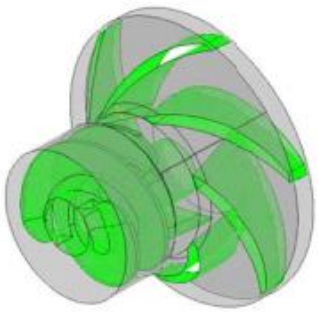

Figure 3 – Meshes on the inducer and impeller surfaces

Table 1 – Generated meshes for numerical simulation

Grid Type	Element Number	Exp. Factor	Orthog. Angle	Aspect Ratio	Flow Coeff.	Head Coeff.
	Million	Max=10	Min=20	Max=10	Rated	Rated
1	2.824	3.94	4.61	2.23	0.068	0.742
2	5.286	1.97	2.18	1.05	0.068	0.717
3	8.065	0.92	1.25	0.56	0.068	0.718

Results of numerical simulations

The numerical simulation of flow in a feed pump was conducted at different flow rates but at the constant rotational speed of 1570 radian per second. First, the simulations were performed in the range of existing experimental data. Then, the newly obtained characteristic curve was compared to the characteristic curve of experimental results. As shown in Figure 4, which presents the pump's three characteristic curves obtained from the three methods, a difference exists between the results of the numerical solution and experimental data. This difference is due to simplifications of the pump's geometry during calculations.

56/ Journal of Aerospace Science and Technology
Vol.16/ No. 1/ Winter-Spring 2023

Turbomachines suffer internal and external losses. The internal losses include hydraulic losses, internal leakage, and wall or disk leakage. The external losses include mechanical losses and external leakage. The original geometry of the pump was simplified through numerical calculations of flow, eliminating some pump elements such as leakage passages, seals, and leakage return passages. As a consequence of this elimination and therefore skipping over leakage and disk losses, the pump became more efficient. So, it is acceptable to have a difference between numerical and experimental results and the numerical results can be adjusted in light of the losses mentioned above. The adjusted results are also demonstrated in Figure 4. During this adjustment, the existing difference at the nominal point was reduced, and some efficiencies were applied to the leakages that were not considered in the simulation.

The nominal flow coefficient equals φ = 0.068. Pressure distribution on the inducer and impeller surfaces is shown in Figure 5. The contour of pressure distribution to the meridional part is demonstrated in Figure 6. As you can see in the figures, most pressure increase occurs in the impeller and inducer. The pressure in the inducer increases to the extent that the flow has enough pressure at the impeller entrance. As shown in Figure 7, which presents flow lines in the pump, flow lines near the tongue of the volute demonstrate a vortex flow.

In Figure 4, the characteristic curve obtained by solving the flow in the range of nominal flow coefficient is presented. To detect the pump's stable performance range, the characteristic curve should be obtained in low flow coefficients. After conducting simulations in the mentioned points and drawing a third- and a fourth-degree curve based on the detected points, the pump's performance curves in different flow coefficients were extracted. Figure 8 presents the curve obtained with the third-degree polynomial, and Figure 9 shows the curve obtained with the fourth-degree polynomial. The following head coefficient equations that are dependent on flow coefficient were developed based on the results of simulations as third- and fourth-degree polynomials.

$$\psi = -349.65\varphi^3 + 44.397\varphi^2 - 1.504\varphi + 0.7234$$

$$\psi = 7962.4\varphi^4 - 2018.2\varphi^3 + 155\varphi^2 - 3.9475\varphi + 0.7336$$

Stable, unstable and transient ranges were determined by graphs of third- and fourth-degree polynomials. That area of the curve with a positive slope was chosen as the stable area. There are two inflection points in the derivation of the head coefficient. The flow coefficient of the unstable area was lower than the flow coefficient of the stable area. In areas with extremely low flow coefficients, the slope of the characteristic curve was negative; however, they were not determined as stable. As described in the Introduction, the flow through these areas is transient. To determine the boundaries between stable, unstable and transient regimes, derivation of head coefficient-flow coefficient relationship was zeroed. In doing this, inflection points of the curve were detected.

As shown in Figure 8, the pump's stable performance is within the range of 0.023 < φ < 0.061 based on the third-degree polynomial fitted on numerical results. In points with a value of more than 0.061, the pump's performance is stable and in points with a value less than 0.023, the pump's performance is transient. As shown in Figure 9, the pump's unstable performance is within the range of 0.019 < φ < 0.057 based on the fourth-degree polynomial fitted on numerical results. In points with a value of more than 0.057, the pump's performance is stable and in points with a value less than 0.019, the pump's performance is transient.

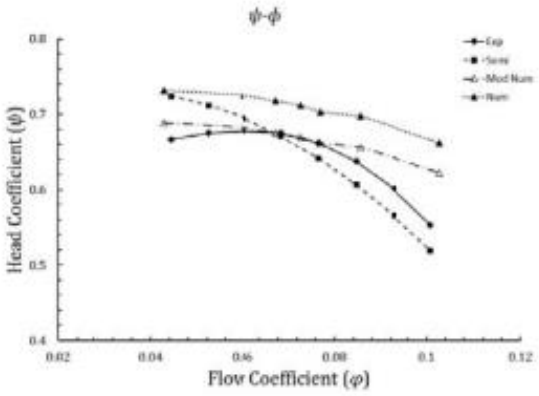

Figure 4 – Pump's characteristic curve and comparison of it with experimental results

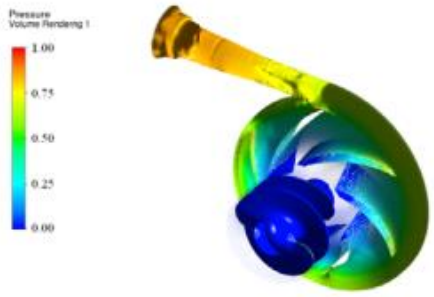

Figure 5 – Pressure distribution on pump

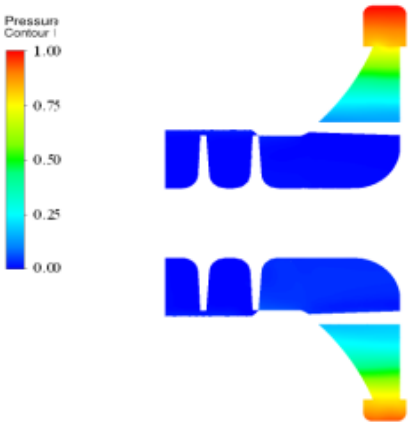

Figure 6 – Pressure distribution on meridional view

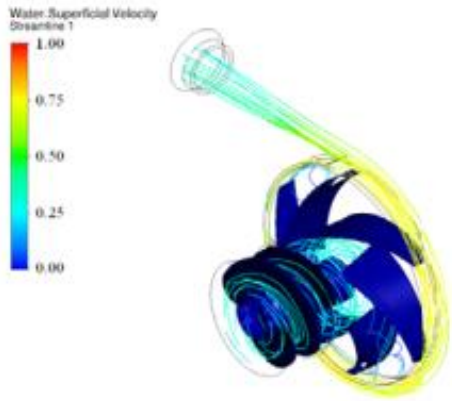

Figure 7 – Streamlines in the Flow-field

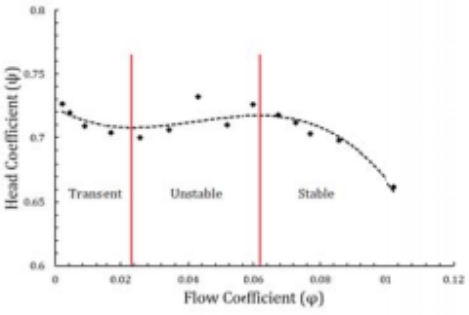

Figure 8 - Determination of the pump's stable performance range based on the third-degree characteristic curve

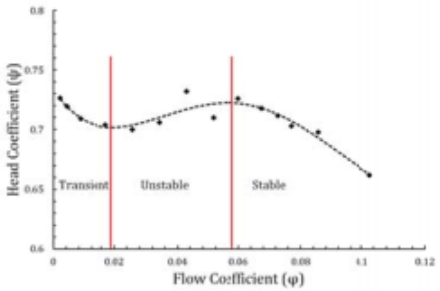

Figure 9 - Determination of the pump's stable performance range based on the fourth-degree characteristic curve

Research implications

The current paper presents flow simulation through a high-speed centrifugal pump. The pump's characteristic curve was obtained based on the numerical simulation results. Numerical results were compared to experimental ones. The existing difference between numerical and experimental results is acceptable due to simplifications of geometry and mesh generating. To determine a pump's different performance ranges, the flow was simulated even at very low flow rates. Stable, unstable and transient performance ranges were determined by extracting the pump's characteristic curve in different ranges of flow rate. The authors of the present study will investigate flow simulation in a pump with cavitation and the effect of cavitation on the pump's characteristic curves in their future research.

References

[1] Brennen C.E., "Hydrodynamics of Pumps," Concepts NREC and Oxford University, 1994.
[2] Grist E., "Cavitation and a centrifugal Pump (A Guide for Pump Users)," Taylor&Francis, 1998.
[3] Coutier-Delgosha O., Reboud J. L., Fortes-Patella R., "Numerical Study of the Effect of the Leading-Edge Shape on Cavitation Around Inducer Blade Sections, "JEME International Journal, Series B, Vol. 45, No. 3, 2002.
[4] Tokumasu T., Sekino Y., Kamijo K., "The Numerical Analysis of the Effect of Flow Properties on the Thermodynamic Effect of Cavitation," Trans. Japan Soc. Aero. Space Sci., Vol. 47, No. 156, 2004.
151 Ugajin H., Watanabe O., Kawai M., Kobayashi S., Tomaru II., Ohta T., "Numerical Simulation of Cavitating Flow in Inducers, "40th AIAA/ASME/SAF/ASEE Joint Propulsion Conference, Fort Lauderdale, 11-14 July 2004.
[6] Pierrat D., Gros L., Pintrand G., Le Fur B., Gyomali Ph., "Experimental and Numerical Investigation of Leading-Edge Cavitation in a Helico-Centrifugal Pump," 12th International Symposium on Transport Phenomena and

Dynamics of Rotating Machinery, Honolulu, Hawaii, February 17-22, 2008.

[7] Yamamoto, K., Tsujimoto Y., "Backflow Vortex Cavitation and Its Effects on Cavitation Instabilities, "International Journal of Fluid Machinery and Systems, Vol. 2, No. 1, January March 2009.

[8] Kang, D., Yonezawa K., Horiguchi H., Kawata Y., Tsujimoto Y., "Cause of Cavitation Instabilities in Three-Dimensional Inducer," International Journal of Fluid Machinery and Systems, Vol. 2, No. 3, July-September 2009.

[9] An Y. J., Shin B. R., "Numerical Investigation of Suction Vortices Behavior in Centrifugal Pump, "Journal of Mechanical Science and Technology, Vol. 25(3), 2011.

[10] Somashekar D., Purushothama H. R., "Numerical Simulation of Cavitation Inception on Radial Flow Pump," IOSR Journal of Mechanical and Civil Engineering, Vol. 1, July-August 2012.

[11] Campos-Amezcua R., Khelladi S., Mazur-Czerwiec Z., Bakir F., Campos-Amezcua A., Rey R., "Numerical and Experimental Study of Cavitating Flow Through an Axial Inducer Considering Tip Clearance," Proc ImechE Part A: 1 Power and Energy, Vol. 227(8), 2013.

[12] Fu Y., Yuan J., Yuan S., Pace G., D'Agostino L., Huang P., Li X., "Numerical and Experimental Analysis of Flow Phenomena in a Centrifugal Pump Operating Under Low Flow Rates, "Journal of Fluids Engineering, Vol. 137, January 2015.

[13] Mishra A., Ghosh P., "Predicting Performance of Axial Pump Inducer of LOX Booster Turbo-pump of Staged Combustion Cycle Based Rocket Engine Using CFD, "IOP Conf. Series: Material Science and Engineering 101, 2015.

[14] Guo X., Zhu Z., Cui B., Shi G., "Effects of the Number Blades on the Anti-Cavitation Characteristics and External Performance of a Centrifugal Pump," Journall of Mechanical Science and Technology, Vol. 30 (7), 2016.

[15] ANSI/API Standard 610, "Centrifugal Pumps for Petroleum," Petrochemical and Natural Gas Industries, 11th Edition, September 2010.

[16] CFX-ANSYS Canada Ltd, Cfx-5.7: "Solver Theory." Canada, 2004.

[17] Versteegand, H. K., and Malalasekera, W., "An introduction to Computational Fluid Dynamics: The finite volume method," vol. Pearson Prentice Hall. 1995.